



HAL
open science

Experiments on fragmentation and thermo-chemical exchanges during planetary core formation

Jean-Baptiste Wacheul, Michael Le Bars

► **To cite this version:**

Jean-Baptiste Wacheul, Michael Le Bars. Experiments on fragmentation and thermo-chemical exchanges during planetary core formation. *Physics of the Earth and Planetary Interiors*, 2018, 276, pp.134-144. 10.1016/j.pepi.2017.05.018 . hal-02068313

HAL Id: hal-02068313

<https://hal.science/hal-02068313>

Submitted on 14 Mar 2019

HAL is a multi-disciplinary open access archive for the deposit and dissemination of scientific research documents, whether they are published or not. The documents may come from teaching and research institutions in France or abroad, or from public or private research centers.

L'archive ouverte pluridisciplinaire **HAL**, est destinée au dépôt et à la diffusion de documents scientifiques de niveau recherche, publiés ou non, émanant des établissements d'enseignement et de recherche français ou étrangers, des laboratoires publics ou privés.

Experiments on fragmentation and thermo-chemical exchanges during planetary core formation

Jean-Baptiste Wacheul^a, Michael Le Bars^a

^a*CNRS, Aix Marseille Univ, Centrale Marseille, IRPHE, Marseille, France*

Abstract

The initial thermo-chemical state of telluric planets was largely controlled by mixing following the collision of differentiated proto-planets. Up to now, most models of planet formation simply assume that the iron core of the impactors immediately broke up to form an “iron rain” within a large-scale magma ocean, leading to the rapid equilibration of the whole metal with the whole mantle. Only recent studies have focused on resolving the fluid mechanics of the problem, with the aim to define more relevant diffusion-advection models of thermal and chemical exchanges within and between the two fluids. Furthermore, the influence of the viscosity ratio on this dynamical process is generally neglected, whilst it is known to play a role in the breakup of the initial iron diapirs and in the shape of the resulting droplets. Here we report the results of analog laboratory experiments matching the dynamical regime of the geophysical configuration. High speed video recording allows us to describe and characterize the fluid dynamics of the system, and temperature measurements allow us to quantify the diffusive exchanges integrated during the fall of the liquid metal. We find that the early representation of this flow as an iron rain is far from the experimental results. The equilibration coefficient at a given depth depends both on the initial size of the metal diapir

and on the viscosity of the ambient fluid, whereas the falling speed is only controlled by the initial size. Various scalings for the diffusive exchanges coming from the literature are tested. We find good agreement with the turbulent thermal model developed by Deguen et al. (2014).

Keywords:

Planet collision, Two phase flow equilibration, Laboratory experiments

1. Introduction

1 The aggregation time scale of moon-size planets in a protoplanetary disk
2 is on the order of 10 to 100 Myr (Chambers, 2004; O’Brien et al., 2006). It
3 is comparable to the typical time scale of differentiation of terrestrial bodies
4 inferred from meteorite analysis (Lee and Halliday, 1996; Kleine et al., 2004)
5 and numerical simulations (Neumann et al., 2012). This implies that Earth
6 and other terrestrial bodies most likely formed from the collision of already
7 differentiated proto-planets (Yoshino et al., 2003). These events were by
8 themselves energetic enough to cause a local melting of the mantle (Safronov,
9 1978; Kaula, 1979; Reese and Solomatov, 2006; Monteux et al., 2007). In
10 addition, there was enough ^{26}Al for the decay heat to elevate the mantle’s
11 temperature above solidus across depths of several hundreds of kilometers
12 (Merk et al., 2002), and thus produce a deep global magma ocean (Tonks
13 and Melosh, 1992).

14 After the impact, the liquid iron from the impactors’ core sank through
15 the molten silicate mantle allowing efficient equilibration, the details of which
16 being a matter of fluid dynamics. Once formed, the core and mantle of
17 terrestrial planets are weakly coupled regarding heat and element exchanges,

18 because the surface of exchange is relatively small and because transfers can
19 only take place through diffusion and very slow advection in the solid mantle.
20 Consequently, the internal dynamics of these reservoirs strongly depend on
21 their initial thermochemical states (Samuel et al., 2010; King and Olson,
22 2011). Also, our understanding of the event chronology taking place during
23 planetary accretion relies on radio-nucleid: loose constraints on metal/silicate
24 partitioning at the very end of accretion don't allow to discriminate between
25 a wide range of possible scenarii (Kleine et al., 2004; Allègre et al., 2008).

26 Past studies provide us with a partial story on the flow occurring after the
27 impact. Provided that the initial mass of liquid metal can be seen as a unique
28 source referred to as a “diapir”, it falls as a turbulent thermal (i.e. an isolated
29 buoyant mass of fluid, in which gravitational potential energy is converted to
30 turbulent motion, causing mixing: see Deguen et al., 2011), breaks-up within
31 a depth of a few diapir's initial radii to capillary-sized droplets (Ichikawa
32 et al., 2010; Samuel, 2012; Wacheul et al., 2014), except for the largest diapirs
33 (Dahl and Stevenson, 2010) or if planetesimals cores undergo massive mixing
34 during their impact (Kendall and Melosh, 2016). Turbulent thermals are
35 dominated by collective effects between droplets, until they transition to an
36 “iron rain” regime when diluted enough (Bush et al., 2003; Deguen et al.,
37 2011). The size and speed of droplets in this last regime allow droplets to
38 fully equilibrate with the ambient silicate well before reaching the bottom
39 of the magma ocean (Stevenson, 1990; Rubie et al., 2003; Ichikawa et al.,
40 2010; Ulvrová et al., 2011; Samuel, 2012). However, the typical length scale
41 required for significant equilibration is very important because it sets the
42 depth, *i.e.* the pressure of equilibration between the metal and silicate.

43 Recent studies (Deguen et al., 2014) suggest that the smallest scales of the
44 induced turbulence, even before fragmentation, could drastically reduce this
45 equilibration length scale. It is then crucial to precisely understand how the
46 fluid mechanics of this flow governs diffusion.

47 We report in the present article the results of laboratory experiments
48 on a fluid system analog to the liquid silicate/ liquid iron system, where
49 we performed measurements of both the fluid dynamics and the thermal
50 diffusive exchanges over the depth of our experimental domain. The set-up
51 and relevant parameters are described in sections 2 and 3 respectively. The
52 fluid dynamics of sedimentation and fragmentation are addressed in section
53 4. Equilibration results are analysed in section 5 in comparison with various
54 models from the literature. Finally, conclusions and future works are shortly
55 reviewed in section 6.

56 **2. Experimental set-up**

57 As shown in figure 1, our set-up consists in a 45x45x100cm polycarbonate
58 tank filled with a mixture of water and UCONTM oil of density 1050 kg.m^{-3} ,
59 that is used here to mimic the molten silicate. Its viscosity can be adjusted
60 over 5 orders of magnitude depending on the mass fraction of water, in order
61 to reproduce the range of viscosity ratios of the liquid iron/silicate magma
62 system at low pressure (Rubie et al., 2003). To mimic the impacting iron core,
63 we use a balloon filled with galinstan, a gallium alloy that is liquid at room
64 temperature. Its surface energy is 0.718 J.m^{-2} , and its density 6440 kg.m^{-3} .
65 Before each experimental run, the mixture water/UCONTM oil is vigorously
66 mixed in order to homogenize the temperature. A balloon is filled with a

67 given mass of galinstan and precisely weighted. A thermocouple is inserted
68 in the balloon before closing it. The balloon is then placed in a hot container
69 in order to heat the galinstan. The viscosity of the mixture water/UCONTM
70 decreases with temperature, therefore the temperature of the galinstan is
71 elevated only by about ten degrees Celsius to avoid lubrication due to higher
72 temperature in the thermal boundary layer. Eventually, the balloon is fixed
73 at the top of the tank where it is immersed in the mixture water/UCONTM
74 oil and popped immediately. The balloon takes only a few thousandths of
75 seconds to retract and the galinstan then starts falling through the viscous
76 fluid. At the bottom of the tank (70 cm below the surface) sits a square funnel
77 made of polystyrene collecting the liquid metal and channeling it towards an
78 adiabatic chamber. When the galinstan is collected, its residual speed mixes
79 completely the temperature and the whole mass of metal reaches an almost
80 constant mean temperature in a few seconds. A thermocouple is placed a few
81 millimeters above the bottom of the adiabatic chamber in order to measure
82 this final temperature. In addition, a third thermocouple is fixed in the
83 middle of the tank one centimeter away from the wall in order to measure
84 the temperature in the bulk of the ambient fluid.

85 For each experimental run, two events are clearly identifiable in the time
86 series of the thermocouples, as seen in figure 2: the release of the galinstan
87 and the moment it reaches the adiabatic chamber at the bottom of the tank.
88 From these signals we compute the temperature drop of the galinstan with
89 respect to ambient fluid during its fall. Each run of the experiment is also
90 recorded by a high speed camera PHOTRON Fastcam at 1000 frames per
91 second with a resolution of 800x1240 pixels.

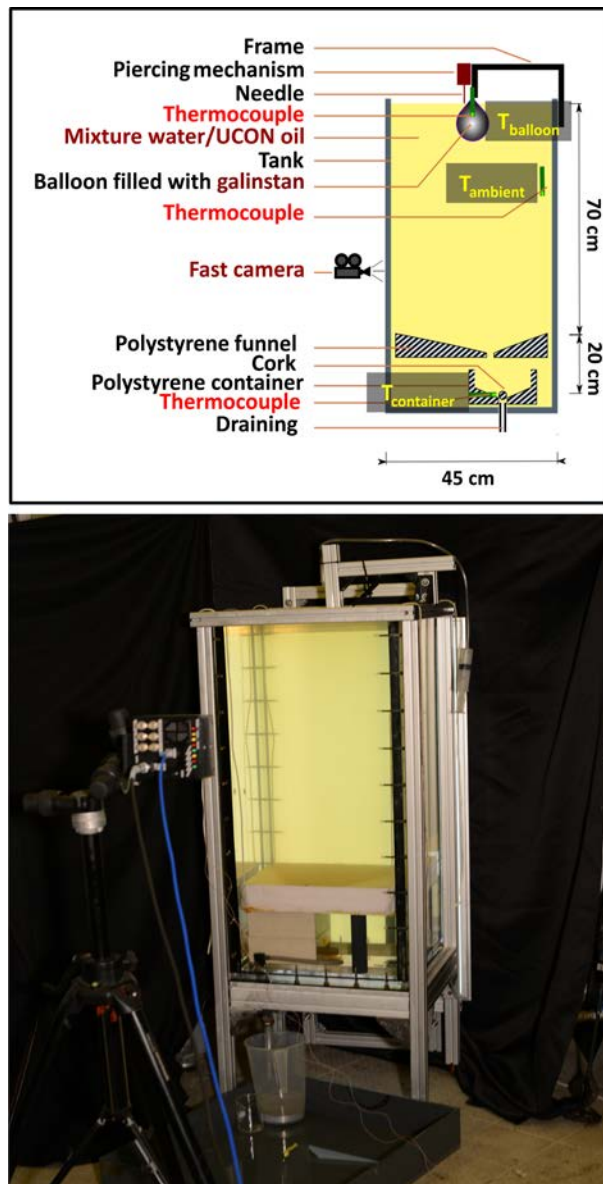


Figure 1: Schematic and picture of the experimental set-up.

92 **3. Parameters and non dimensional numbers**

93 It is still unclear how the initial size of impacting planetesimal converts
 94 into the typical size of liquid iron structures at the surface of the magma

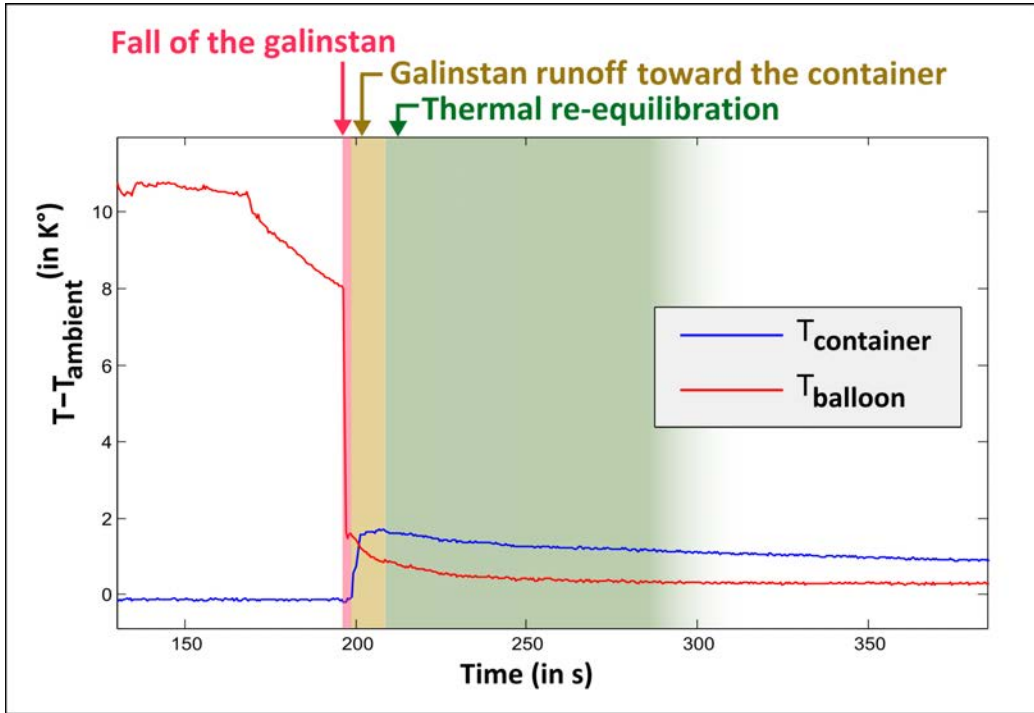


Figure 2: Example of temperature measurements: time series of the temperature difference between the ambient fluid recorded at the initial location of the balloon and in the adiabatic container at the bottom of the tank.

95 ocean just after the impact (Canup, 2004). However, it is very likely that
 96 this typical size depends on the angle of the impact, since stretching and
 97 dilution of the core become very important when the impact is far from the
 98 vertical direction (Kendall and Melosh, 2016). In our approach, we consider
 99 this typical size as a free parameter, and correspondingly we vary the initial
 100 radius of our balloon of galinstan. The other free parameter is the viscos-
 101 ity of the ambient fluid, because the magma viscosity is very dependent on
 102 temperature, composition and pressure (Karki and Stixrude, 2010). It is ad-
 103 justed in our set-up by changing the amount of water in the ambient fluid.

Symbol	Definition	Value / range in our experiment
R_0	initial diapir's radius	0.014 – 0.031 <i>m</i>
μ_a	dynamic viscosity of the ambient fluid	10^{-3} – 1.67 <i>Pa.s</i>
μ_m	dynamic viscosity of the liquid metal	$2.4 \cdot 10^{-3}$ <i>Pa.s</i>
ρ_a	density of the ambient fluid	1050 <i>kg.m⁻³</i>
ρ_m	density of the liquid metal	6440 <i>kg.m⁻³</i>
λ_a	heat conductivity of the ambient fluid	0.45 <i>W.K⁻¹.m⁻¹</i>
λ_m	heat conductivity of the metal	16.5 <i>W.K⁻¹.m⁻¹</i>
Cp_a	heat capacity of the ambient fluid	1500 <i>J.K⁻¹.kg⁻¹</i>
Cp_m	heat capacity of the liquid metal	337 <i>J.K⁻¹.kg⁻¹</i>
g	acceleration of gravity	9.81 <i>m.s⁻²</i>
σ	surface energy	0.718 <i>J.m⁻²</i>
u	typical flow velocity (measured experimentally)	0.6 – 1 <i>m.s⁻¹</i>

Table 1: Definition and experimental range of the variables used in this paper.

104 The two-phase buoyancy-driven flow, theoretically described by the Navier-
105 Stokes and Laplace pressure equations, is then fully characterized by five
106 dimensionless numbers, derived from the parameters listed in table 1:

$$Re = \frac{\rho_a \cdot u \cdot R_0}{\mu_a} ; \quad We = \frac{\rho_a \cdot u^2 \cdot R_0}{\sigma} ; \quad Bo = \frac{(\rho_m - \rho_a) \cdot g \cdot R_0^2}{\sigma} ; \quad (1)$$

$$R_\mu = \frac{\mu_a}{\mu_m} ; \quad R_\rho = \frac{(\rho_m - \rho_a)}{\rho_a}. \quad (2)$$

107 From left to right and up to down, the Reynolds number is the ratio of
108 the flow's inertia over the viscous forces; the Weber number is the ratio of

109 the flow's inertia over the surface tension; the Bond number is the ratio of
 110 the buoyancy forces over the surface tension; and the last two numbers are
 111 the viscosity ratio and the density anomaly.

112 We suppose (and we will prove later using experimental results) that the
 113 inertial forces are in balance with the buoyancy forces over most part of the
 114 flow. This balance sets the order of magnitude of the flow speed, known as
 115 the Newtonian terminal velocity and corresponding to the inviscid free fall
 116 speed

$$u \sim \left(\frac{(\rho_m - \rho_a) \cdot g \cdot R_0}{\rho_a} \right)^{\frac{1}{2}}. \quad (3)$$

117 This scaling implies that the Bond number is proportional to the Weber
 118 number, their ratio being equal to the drag coefficient

$$Cd = \frac{(\rho_m - \rho_a) \cdot g \cdot R_0}{\rho_a \cdot u^2}. \quad (4)$$

119 Cd will be determined experimentally in the following.

120 The ranges of dimensionless parameters explored in our set-up are given in
 121 table 2. As an example for comparison, a planetesimal core of radius 100 km
 122 falls at a typical velocity of 10^3 m.s^{-1} , giving a Reynolds number of about
 123 10^{11} and a Weber number of about 10^{15} . While it is impossible to reproduce
 124 exactly the planetary regime in the laboratory, our set-up allows exploring
 125 the relevant range of dynamical parameters, *i.e.* $Re \gg 1$ meaning that the
 126 flow is highly turbulent and dominated by inertia, and $We \gg 1$ meaning
 127 that the initial diapir is prone to fragmentation. Our experiment can also be
 128 regarded as a close up to the scales where surface tension and viscous forces
 129 both matter and affect the advection-diffusion process, see also our previous
 130 study Wacheul et al. (2014). The expected range of viscosity ratio on Earth

Symbol	Dimensionless parameter	Explored range
Re	Reynolds number	$10^0 - 3.10^4$
We	Weber number	$10^1 - 4.10^1$
R_μ	Viscosity ratio	$4.10^{-1} - 7.10^2$
R_ρ	Normalized density difference	5

Table 2: Values of the dimensionless numbers explored with our set-up.

131 is $10^{-2} - 10^5$, corresponding to regimes which are satisfyingly matched by the
 132 experiments. Note that the normalized density anomaly of our fluid system is
 133 5, larger than the corresponding planetary value of about 1.3. In both cases
 134 however, the density contrast is globally of order 1, meaning that ambient
 135 and metal densities are of the same order of magnitude, with clear non-
 136 Boussinesq effects: we thus expect both cases to be in the same dynamical
 137 regime.

138 Note finally that although the proper way to describe the fall and frag-
 139 mentation of the liquid metal in a viscous fluid involves all dimensionless
 140 numbers described above, the experimental results below will also be de-
 141 scribed in terms of the dimensional parameters R_0 and μ_a , which are the two
 142 adjustable parameters in our set-up.

143 4. Dynamics of the fall

144 Series of snapshots from raw videos of the experiments are presented in
 145 figure 3 for different viscosity ratios. These pictures show several features of
 146 importance when considering the diffusion advection process over the whole
 147 fall. First, we observe that the flow is always turbulent after falling over a

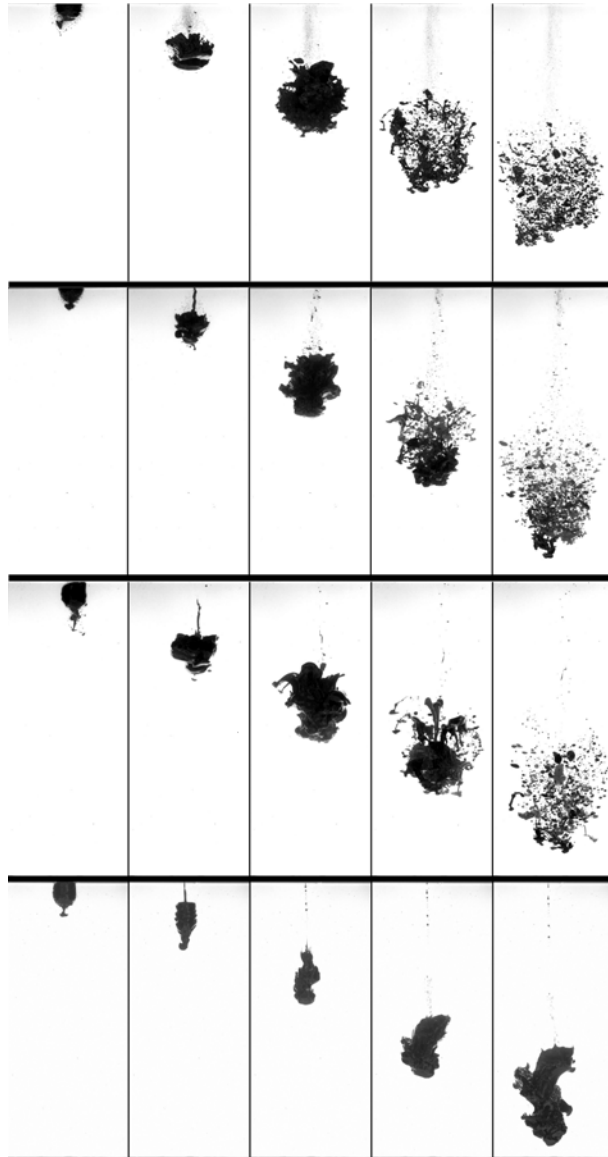


Figure 3: Series of snapshots taken 0.13 s apart from videos of experiments with a 31 mm galinstan diaphragm falling through a viscous fluid with different viscosities: from top to bottom, $R_\mu = 0.383$, $R_\mu = 8.37$, $R_\mu = 72.5$ and $R_\mu = 691$, corresponding respectively to $Re = 34000$, $Re = 1700$, $Re = 195$ and $Re = 20$, with $We = 51$ in all cases.

148 distance equal to 2 radii of the initial diapir, which also corresponds to the
149 length needed to develop strong corrugation of the surface. Our study focuses
150 on the following dynamics. It is also clear from figure 3 that while the ambi-
151 ent viscosity changes over 3 orders of magnitude, the overall falling velocity
152 of the metal remains about the same. This means in our view that our exper-
153 iments are always in the Newtonian regime, i.e. that their falling dynamics
154 is dominated by inertia and largely independent of viscous dissipation. How-
155 ever, it is also clear that the fragmentation process strongly depends on the
156 ambient viscosity: in our view, this is a consequence of the stress continuity
157 at the metal / ambient fluid interface. Hence, and even if strictly speaking,
158 changing the ambient viscosity leads in our set-up to changes both in the
159 Reynolds number and in the viscosity ratio, observed results are interpreted
160 in the following as a function of the viscosity ratio only, tacitly assuming
161 that the Reynolds number is always large (as for planetary applications).

162 *4.1. Dilution of the liquid metal*

163 The dilution of the galinstan mass during its fall seems consistent with the
164 representation of Deguen et al. (2011), at least for the three lower viscosity
165 ratios explored here (*i.e.* $R_\mu \leq 72.5$ at least). For these viscosity ratios, the
166 diapir starts deforming on the sides, presenting oscillations of its interface
167 with the ambient fluid because of Kelvin-Helmholtz instabilities (KH). Vor-
168 tices grow as an evolution of these instabilities and incorporate fluid into the
169 region occupied by the liquid metal. This region grows like a spheroid with
170 a radius apparently increasing linearly with depth, even after the galinstan
171 has broken up in droplets. This is consistent with the classical hypothesis of
172 Morton et al. (1956) concerning turbulent entrainment into a buoyant vol-

173 ume of fluid, which states that the rate of entrainment is proportional to the
 174 mean fall speed. It follows from this assumption that the radius of the region
 175 occupied by the buoyant fluid grows linearly with the depth of this region,
 176 regardless of the speed at which it falls (see Deguen et al. (2014) for details
 177 on the non-Boussinesq turbulent thermal model). We tested this hypothesis
 178 using the images extracted from the videos and binarized according to an
 179 intensity threshold. We measured the barycenter of the black pixels (*i.e.*
 180 containing metal) and we assumed that its depth is the same as the actual
 181 center of mass of the liquid metal. We also measured the standard deviation
 182 of the distance between black pixels and the barycenter of the black pixels,
 183 and assumed that it is proportional to the spherical equivalent radius of the
 184 region occupied by the galinstan. This radius and its derivative with respect
 185 to the depth of the center of mass are shown in figure 4. About 40 experimen-
 186 tal videos containing an average of 700 frames were used for each ambient
 187 fluid’s viscosity to calculate this derivative. For the two lowest viscosity ra-
 188 tios, this derivative is almost constant with depth and reaches a mean value
 189 of $\alpha = \frac{dr}{dz} \simeq 0.19$, which is close to the values usually found for the coeffi-
 190 cient of entrainment for turbulent thermals of particle suspension, ranging
 191 from 0.1 to 0.35 (Bush et al., 2003). In summary, for these viscosity ratios
 192 the apparent expansion of the liquid metal before and after the breakup is
 193 compatible with the scenario of an evolution as turbulent thermals.

194 Figure 4 also shows a different behavior for the larger viscosity ratio:
 195 there, the initial z-derivative of the radius is smaller than for the other cases,
 196 and strongly increases during the fall. The falling diapir clearly does not
 197 evolve as a turbulent thermal. This confirms the direct observations on figure

198 3 : for this large viscosity ratio, the KH instabilities are rapidly saturated
199 and the ambient fluid is not incorporated efficiently in the galinstan. Instead,
200 the galinstan and the mixture water/UCONTM are stretched and form scales
201 that slide on each other, accommodating the shear while minimizing viscous
202 damping (see a close-up in figure 5). The scales are eventually drained in
203 such a manner that very few galinstan separates from the bulk mass. Massive
204 and unique breakup event is not the general breakup mode, in contrast to
205 the 3 other viscosity ratios.

206 The evolution of the radius for $R_\mu = 72.5$ appears to be intermediate
207 between the two extreme trends described above. Nevertheless, the breakup
208 mode is much more similar to the lowest viscosity case. A closer look at the
209 videos of the experiments at $R_\mu = 72.5$ gives an explanation for why the
210 apparent evolution of the radius is leaning both ways, while the majority of
211 the liquid metal breaks up in a burst: indeed this case shares with the one at
212 large viscosity ratio long stretched sheets that develop on the side, are peeled
213 away, and destabilized by Rayleigh-Taylor instability. These structures are
214 common at $R_\mu = 691$ and rare at $R_\mu = 72.5$, but they still make the area
215 occupied by the liquid metal larger. Despite the corresponding rather large
216 discrepancy shown in measurements of entrainment rate in figure 4, we
217 conclude that the turbulent entrainment hypothesis stands for $R_\mu = 72.5$ as
218 for the two lowest viscosity ratios.

219 Using a similar set-up (but without significant variation of the viscos-
220 ity ratio), Landeau et al. (2014) mapped a regime diagram of the breakup
221 regime. Following their classification, our experiments lie between a regime
222 where numerous ligaments are stretched and breakup (jellyfish regime) and a

223 regime where fragmentation is mainly due to the growth of Rayleigh-Taylor
224 instabilities (RT piercing regime). For our lower radii, the fragmentation
225 indeed proceeds in a very similar way to the jellyfish regime. For our higher
226 radii with the higher viscosity ratio, the fragmentation proceeds with RT-
227 instabilities and erosion by shear, which can be seen as a transition between
228 the jellyfish and the RT piercing regimes. However, for our higher radii
229 with the 3 lower viscosity ratios, the growth of RT instabilities is generally
230 very limited and they are often advected at the back of the liquid metal
231 mass. Their full development is more occasional than in the experiments of
232 Landeau et al. (2014). This may be due to the higher density ratio in our
233 experiments, inducing a much higher initial acceleration that could reduce
234 the growth rate of the instabilities and enhance the advection of these per-
235 turbations. This effect clearly deserves more study, but is beyond the scope
236 of the present paper.

237 *4.2. Fall velocity*

238 From the same series of movies, we computed the velocity of the metal
239 diapir (or of the droplets cloud after breakup) by assuming it equates the
240 speed of the barycenter of the black pixels. Some examples of computed
241 barycenter depth as a fonction of time are shown in figure 6. The veloc-
242 ity is almost constant over the entire fall of each diapir, including after its
243 breakup. We expect that over a longer distance, droplets may finally be-
244 have independently and not as a cloud anymore, in which case the global
245 barycenter velocity would be meaningless. Note that this effect is quantified
246 by the so-called Rouse number, equal to the ratio of a single particle terminal
247 velocity in a quiet infinite medium over the velocity of the flow it is caught

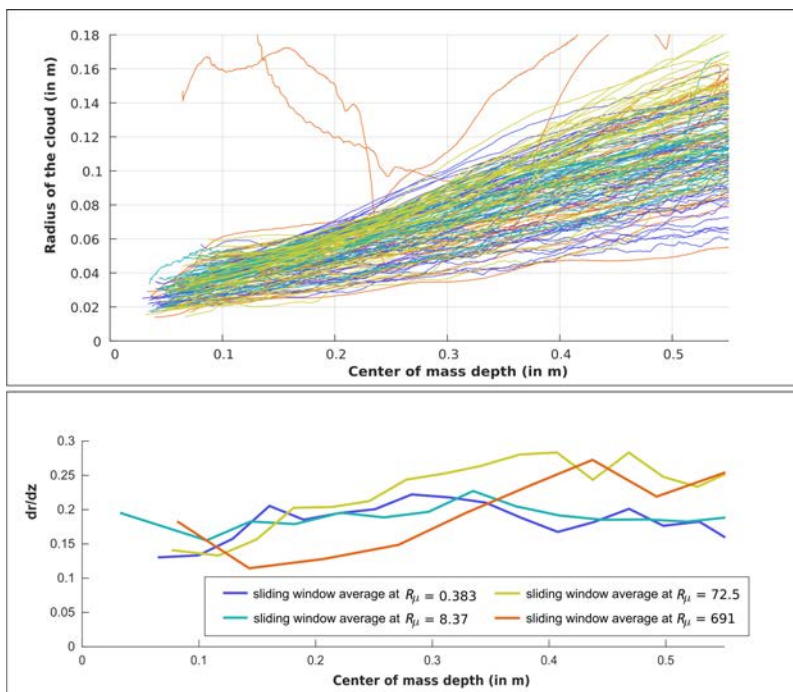


Figure 4: **Top:** Radius of the region occupied by the liquid metal measured from video analysis as a function of the depth z of the center of mass of the liquid metal for all experiments. **Bottom:** z -derivative of the radius of the region occupied by the liquid metal averaged between all the experiments at the same viscosity ratio. The color scale for both plots corresponds to the different viscosity ratios, as given in the bottom plot.

248 in. The Rouse number determines if a cloud of droplet behave collectively
 249 ($Rouse \ll 1$) or if the droplets fall independently as they would in an infinite
 250 medium ($Rouse \gg 1$). For our experiments, the Rouse number is between
 251 $1/3$ and $1/2$.

252 We show on figure 7 our measures of the drag coefficient Cd , *i.e.* the
 253 square of the ratio between the inviscid free fall speed scaling over the mea-
 254 sured mean velocity, as defined in equation (4). Cd is almost constant over
 255 the explored range of Reynolds number, including experiments with the high-



Figure 5: Snapshot of the fall of a 24 mm diapir in the most viscous ambient fluid $R_\mu = 691$. This corresponds to $Re = 14$, with $We = 31$; this is an example of a diapir that does not burst although it is above the critical radius for breakup limited by surface tension (Hinze, 1955).

256 est ambient viscosity: inertia always dominates the flow. The mean value of
257 Cd is $Cd = 3.7 \pm 1$. This value is larger than those for rigid objects at cor-
258 responding Reynolds numbers, which are typically around or below 1 (Clift
259 et al., 1992). Such a high value, corresponding to a lower effective falling
260 velocity, is presumably related to the higher area of the diapir's cross flow
261 surface since it deforms easily.

262 For comparison, the theoretical speed of a turbulent thermal developed
263 in Deguen et al. (2014) is also shown in figure 6. The agreement with our
264 experimental results is reasonably good, at least within the uncertainty of

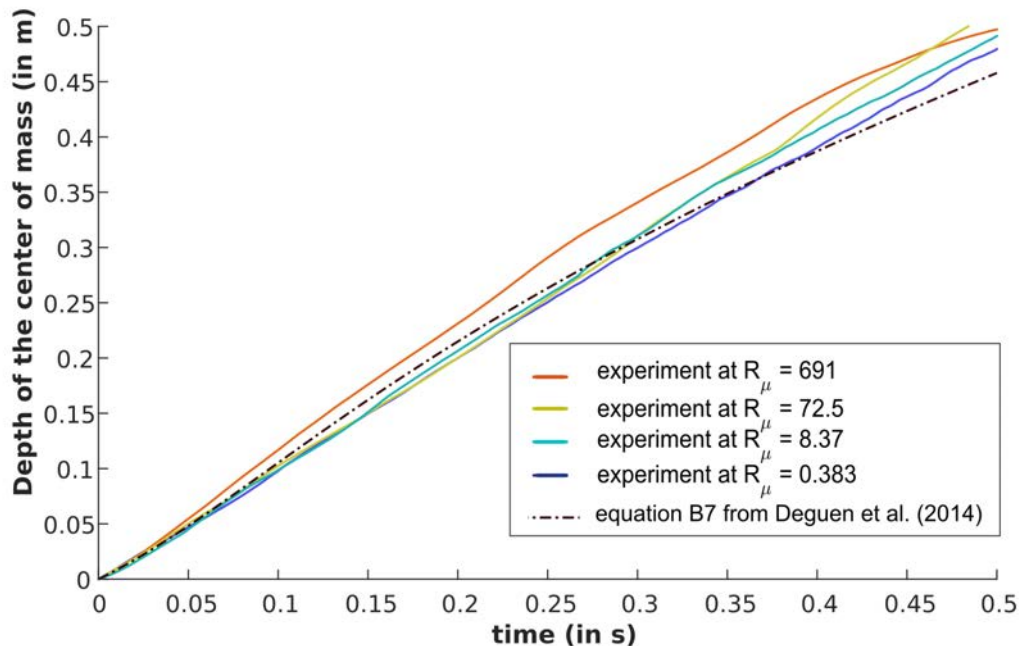


Figure 6: Depth of the galinstan center of mass as a function of time measured during one run for each viscosity ratio, starting from a 31 mm initial radius diapir. From the lowest viscosity ratio to the highest, this corresponds to $Re = 34000$, $Re = 1700$, $Re = 195$ and $Re = 20$, with $We = 51$ for each case. For comparison, we also show the results of the turbulent thermal model equation of Deguen et al. (2014) integrated in time, using the parameters found by Deguen et al. (2014) (dashed dotted line). The initial speed of the turbulent thermal is set to the speed calculated from the videos.

265 our data. We nevertheless claim that our experiments do not exhibit the
 266 deceleration predicted by the turbulent thermal model. Two explanations
 267 for this discrepancy could be provided. First, as mentioned above, the Rouse
 268 number is between $1/3$ and $1/2$, which means that drops behave collectively
 269 but they may not impart their momentum to the ambient with a maximum
 270 efficiency as a cloud of droplets with a very low Rouse number would. Sec-

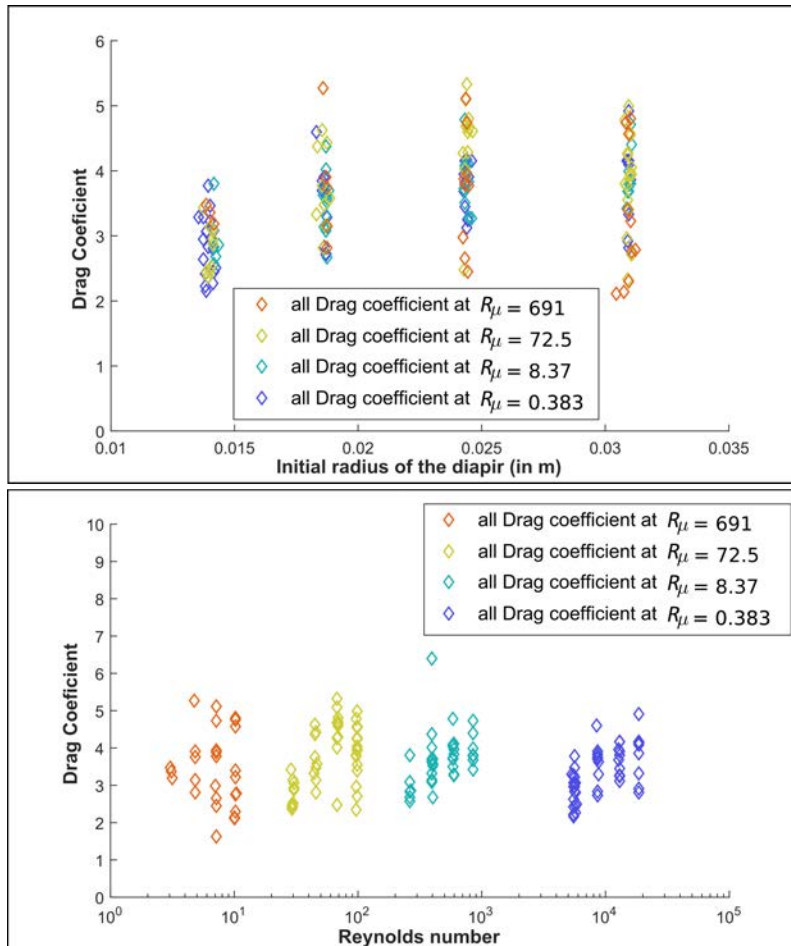


Figure 7: **Top:** Drag coefficient measured from video analysis as a function of the initial radius of the diaphragm for each experiment. **Bottom:** Drag coefficient as a function of the Reynolds number.

271 ondy, we also argue that some physics may be missing in the thermal model,
 272 especially before break up. There, engulfment of the ambient fluid happens
 273 mostly at the rear of the diaphragm (see figure 3). This flux produces an ex-
 274 pansion of the liquid metal sheet that works against surface tension. This
 275 corresponds to an over-pressure in the liquid that is entrained in the liquid

276 metal, much similar to a balloon. This pressure could force the previously en-
277 trained liquid out of the envelope made by the liquid metal sheet. This could
278 result in a linear expansion of the region occupied by the liquid metal with
279 depth, simultaneously with a non-zero flux of momentum associated with the
280 entrainment. This is the main difference with a turbulent thermal, whose
281 equations of movement are based on the assumption that entrainment adds
282 mass with no momentum, the momentum of the buoyant liquid being glob-
283 ally redistributed, leading to a global speed reduction. This explanation for
284 the constant speed cannot be tested for the moment because it requires pre-
285 cise velocimetry of the ambient fluid surrounding the diapir before it breaks
286 up. Nevertheless, it does not question the validity of the assumptions made
287 for the diffusive-advective process of heat in an unbroken turbulent thermal
288 made by Deguen et al. (2014), as they rely on the turbulent nature of the
289 flow and on the apparent radius of the liquid metal mass. We will test these
290 scalings in section 5.

291 *4.3. Breakup distance*

292 For the highest viscosity case, fragmentation proceeds with “slices” of liq-
293 uid metal that are peeled away, and by successive division of the initial diapir
294 in several branches, which makes the breakup progressive. On the contrary,
295 the experiments with $R_\mu \leq 72.5$ present one big burst as a consequence of
296 the intense stretching that the galinstan undergoes when incorporating the
297 ambient fluid. The metal becomes a very thin sheet highly convoluted, which
298 is suddenly pierced with many holes. Those holes grow until forming liga-
299 ment when two holes collide. Each ligament then breaks up as a result of
300 Rayleigh-type capillary instabilities (Lasheras et al., 1998). This mode of

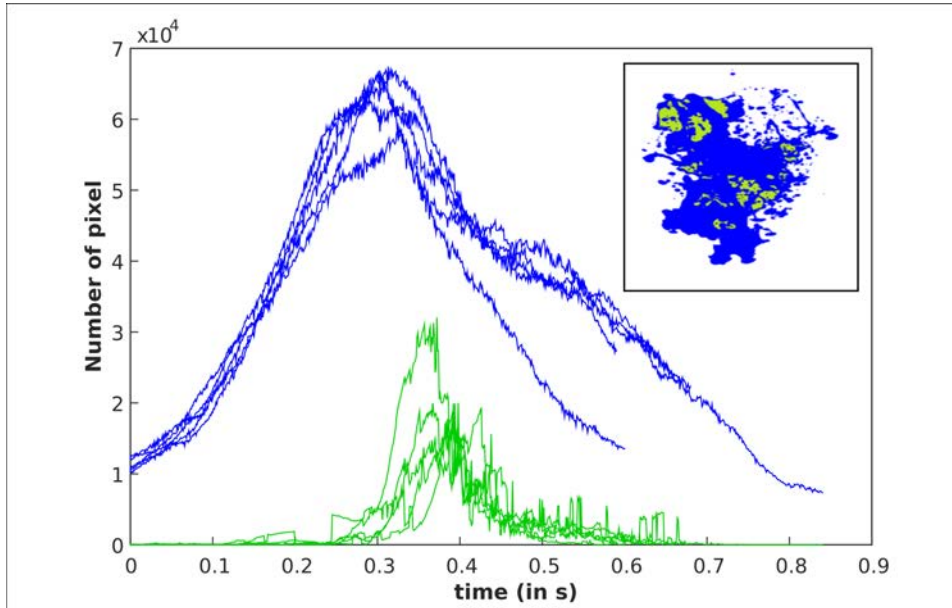


Figure 8: Number of black pixels (blue) and number of white pixels enclosed in a region of black pixels (green) in each frame as a function of time for several videos of the fall of a 0.031 m radius diapir in a water/UCONTM oil corresponding to $R_\mu \leq 72.5$. The inset shows a colored snapshot from one video, imaging those two computed quantities using the same color code.

301 fragmentation allows us to define a quantitative breakup criterion. We de-
 302 fine the breakup as the moment when most of the liquid metal sheets have
 303 retracted from the holes. In order to compute a breakup distance, we mea-
 304 sured several quantities on the binarized images extracted from the video
 305 that we assume are affected by this changing topology. These are (see an
 306 example figure 8): the quantity of black pixels, the absolute value of its time
 307 derivative, and the quantity of white pixels that are enclosed in a black pixel
 308 region (a hole). We then compute the following variable as a function of

309 depth:

$$K(z) = nb_{bl}^a * nb_{ho}^b * \left(\frac{dnb_{bl}}{dt} \right)^c, \quad (5)$$

310 where nb_{bl} is the number of black pixels, nb_{ho} is the number of white pixels
311 in the regions enclosed by black pixels, and a , b and c are positive exponents.
312 We finally define the breakup depth as the first depth of the barycenter of
313 black pixels at which this variable K reaches half its maximum. From our
314 experience, fixing a threshold value of half the maximum of the variable K
315 is necessary to avoid spurious maxima that sometimes appear, for instance
316 when the cloud of droplets reaches the bottom of the set-up. The variation
317 of this measured depth is reported in figure 9, non-dimensionnalised by the
318 initial radius of the diapir. The choice of the breakup criterion and of the
319 weighting exponent a , b and c is arbitrary: it was chosen so as to minimize
320 the noise from the experimental data. But even though it is arbitrary, the
321 results presented in figure 9 are only weakly sensitive to this choice. Thus this
322 simple criterion based on light intensity and topology seems robust enough
323 to give meaningful trends.

324 The smallest diapirs give much dispersed results, because of the weaker
325 probability to record a hole visible on the video. Increasing the mass gives
326 more chance to record holes, which makes our criterium better suited for large
327 diapirs, with a better statistical convergence. Yet a significant variability is
328 still observed, even for the largest diapirs: it corresponds in our view to the
329 natural variability of such non-linear dynamics. Note also again that for
330 our lowest Reynolds data points (i.e. highest viscosity), the breakup distance
331 does not correspond to a clear transition from a single coherent mass to a
332 cloud of droplets: our criteria nevertheless indicates a characteristic distance

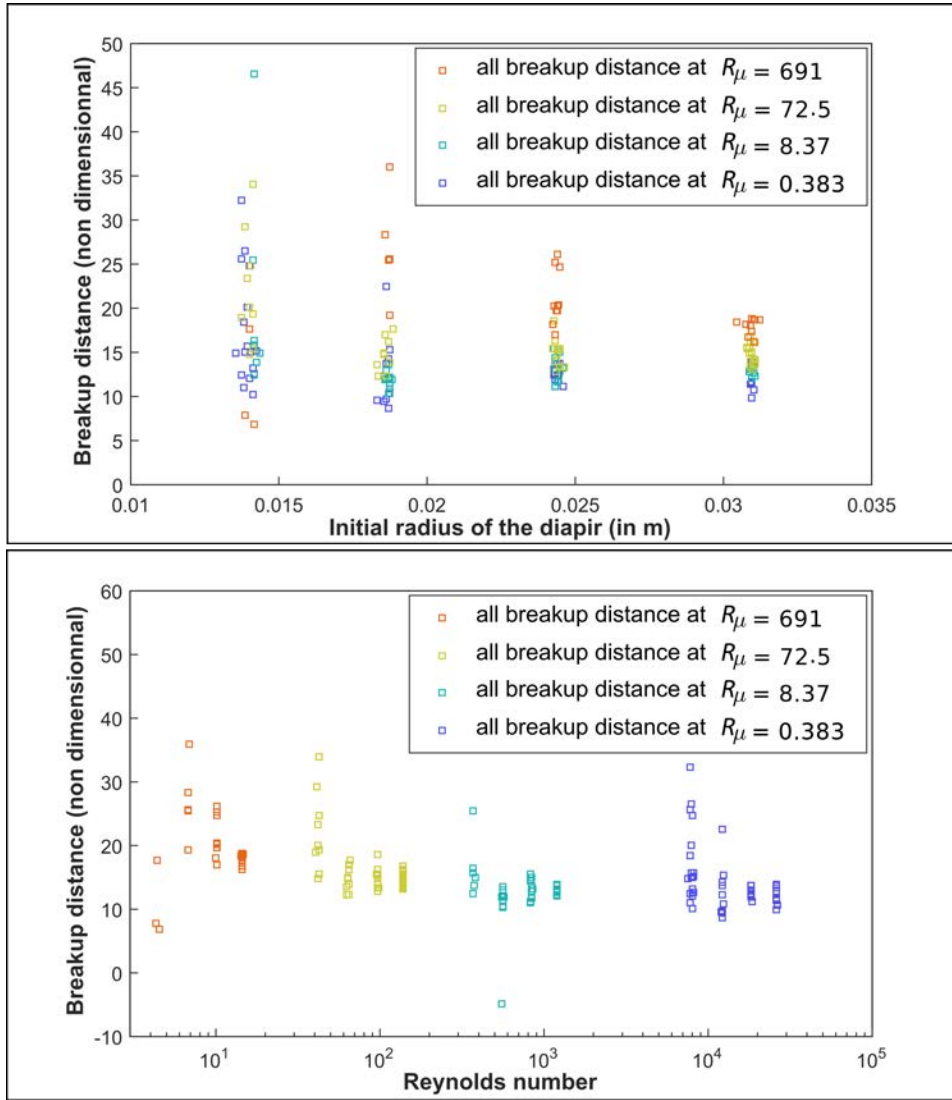


Figure 9: **Top:** Breakup distance (divided by the initial radius) computed from video analysis as a function of the initial radius of the diapir for each experiment. **Bottom:** Breakup distance as a function of the Reynolds number.

333 for a significant change of topology, that will deserve additional study. Here
 334 we focus below on the three largest Reynolds numbers that give a clear trend:

335 the breakup distance L_{bk} is proportional to the initial radius, as expected in
 336 the literature (Deguen et al., 2011; Samuel, 2012). We also see here that it
 337 weakly depends on the viscosity ratio. From figure 9, one could use a mean
 338 value $L_{bk}/R_0 = 13 \pm 2$.

339 To explain this proportionality, let us assume that the region occupied
 340 by the galinstan stays dense (in the mathematical sense) when incorporating
 341 ambient fluid in the region of space it occupies on the video (i.e. the largest
 342 domain around the barycenter of black pixels where metal is present). Then,
 343 the mean stretching undergone by a galinstan fluid particle has to be a grow-
 344 ing function of the volume fraction of the ambient fluid in the region occupied
 345 by the galinstan. In that case, the diapir deforms and incorporates more and
 346 more ambient fluid, until it reaches a critical volume fraction: there, struc-
 347 tures are stretched to such an extent that capillary instabilities grow faster
 348 than stretching. Let's assume there is a critical volume fraction Φ_{bk} that
 349 does not depend on the initial radius. By conservation of the total volume of
 350 galinstan, it can be written with the initial radius R_0 and the radius of the
 351 region occupied by the galinstan when the breakup occurs R_{bk}

$$\Phi_{bk} = \left(\frac{R_0}{R_{bk}} \right)^3 \Rightarrow R_{bk} = R_0 \cdot \Phi_{bk}^{-\frac{1}{3}} \quad (6)$$

352 As shown in section 4.1, the depth and the radius are proportional, with
 353 $\alpha = 0.19$ the mean derivative of the radius with respect to depth, determined
 354 in figure 4. The breakup distance L_{bk} can be written as

$$L_{bk} = \alpha^{-1}(R_{bk} - R_0) = \alpha^{-1} \cdot R_0 \cdot (\Phi_{bk}^{-\frac{1}{3}} - 1), \quad (7)$$

355 With our experimental results, we find $\Phi_{bk} = 0.0239 \pm 0.01$. Viscosity is

356 expected to slow down the dynamics of thin fluid sheets (Villermaux et al.,
 357 2013): this implies a smaller critical volume fraction for a larger viscosity
 358 contrast, hence a larger breakup distance, in agreement with the the small
 359 global increase at low Reynolds number that might be noticed in figure 9. But
 360 we don't have yet a sufficient resolution to quantify this effect. Obviously, the
 361 details of the break-up have to be addressed by further studies of the small
 362 scale fluid mechanics happening during this extremely fast event. For now,
 363 we suggest the use of the breakup distance shown in figure 9 for simulations
 364 of planet accretion that consider a post-impact initial condition with a given
 365 length scale.

366 4.4. Droplet size

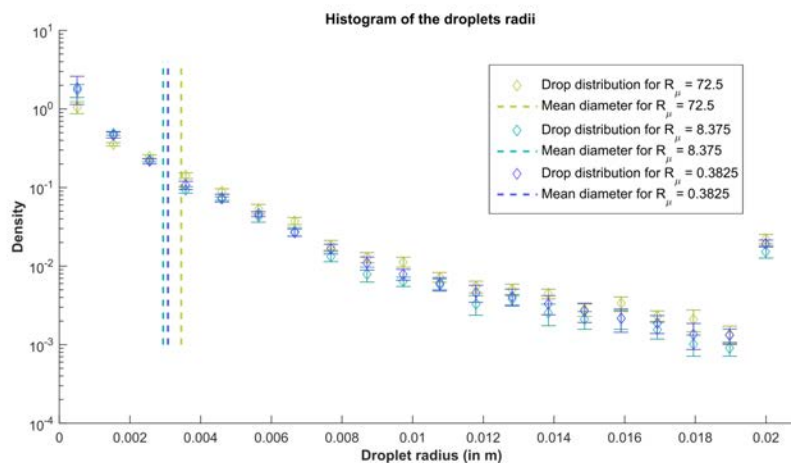


Figure 10: Average histogram of the droplets sizes (bin size 1mm) measured on the videos of a 20 mm radius diapir for the three lowest viscosity ratios. From the lowest viscosity ratio to the highest, this corresponds to $Re = 15900$, $Re = 790$, and $Re = 91$, with in each case $We = 18$. Each of these histograms results from 6 runs, analyzing for each run the last 20 frames before the diapir reaches the bottom of the experiment.

367 The same analysis of the droplets radius distribution as in our previous
 368 study (Wacheul et al., 2014) has been conducted. A better imaging of the
 369 experiment in the present set-up enables us to analyze the three lowest vis-
 370 cosity ratios. For $R_\mu = 691$, a converged distribution of sizes for stable drops
 371 was unaccessible, as only a small fraction of the liquid metal was contained
 372 in stable structures. Distributions of sizes for droplets coming from a 20
 373 mm radius diapir are shown in figure 10: it shows a mean radius around
 374 3.5 ± 1 mm, with no clear or systematic trend with the viscosity. This value
 375 agrees well with the length scale at which surface tension equilibrates the
 376 dynamic pressure due to turbulence l_σ (Hinze, 1955)

$$l_\sigma = R_0 \cdot We^{-\frac{3}{5}}. \quad (8)$$

377 For our experiment, this length scale is about 3 mm. Note that this value
 378 is commonly used to estimate the mean radius of fragments resulting from
 379 turbulence in a diluted two phase flow (Kolmogorov, 1949; Hinze, 1955; Chen
 380 and Middleman, 1967). As already suggested in Deguen et al. (2014), we
 381 support the use of this scaling rather than the classical “laminar” capillary
 382 length scaling

$$l_\sigma^{lam} = R_0 \cdot We^{-\frac{1}{2}} \simeq 4.5mm. \quad (9)$$

383 5. Equilibration

384 Let us define the experimental degree of equilibration:

$$T^*(z) = \frac{T_{initial} - T(z)}{T_{initial} - T_{ambient}} \quad (10)$$

385 where $T_{initial}$ is the initial temperature of the galinstan, $T_{ambient}$ is the tem-
386 perature of the mixture water/UCONTM, and $T(z)$ is the mean temperature
387 of the galinstan at depth z .

388 The experimental degrees of equilibration are shown in figure 11. For
389 reference, this figure also shows the prediction for the degree of equilibration
390 assuming total thermal equilibration between the mass of metal and a finite
391 volume of the ambient fluid. The calculation was made with two volumes:
392 the volume of ambient fluid that a turbulent thermal with a coefficient of
393 entrainment $\alpha = 0.15$ incorporates, corresponding to the most conservative
394 estimate of α from our experiment, and the volume of ambient fluid that a
395 turbulent thermal with a coefficient of entrainment $\alpha = 0.19$ incorporates,
396 which is the average value of α from our experiments. The fact that the
397 experimental degrees of equilibration are all below the predicted ones proves
398 that no full equilibration can be expected, therefore a good understanding
399 of the fluid mechanics is needed to model the exchanges between the two
400 phases, as already claimed by Deguen et al. (2014).

401 Most models of terrestrial planet formation require a length scale of equi-
402 libration as they consider potential temperatures and partition coefficients as
403 a function of depth (see e.g. Boujibar et al., 2014). The length scale of equi-
404 libration allows the quantification of the precise conditions in temperature
405 and pressure relevant for the equilibration of the liquid metal with the silicate
406 magma. In order to compute such a length scale from our experiments, we
407 use the diffusion equation, stating that the heat flux lost by a diapir is pro-
408 portional to the temperature difference between its interior and the ambient
409 fluid, and inversely proportional to the size of the diffusive boundary layer

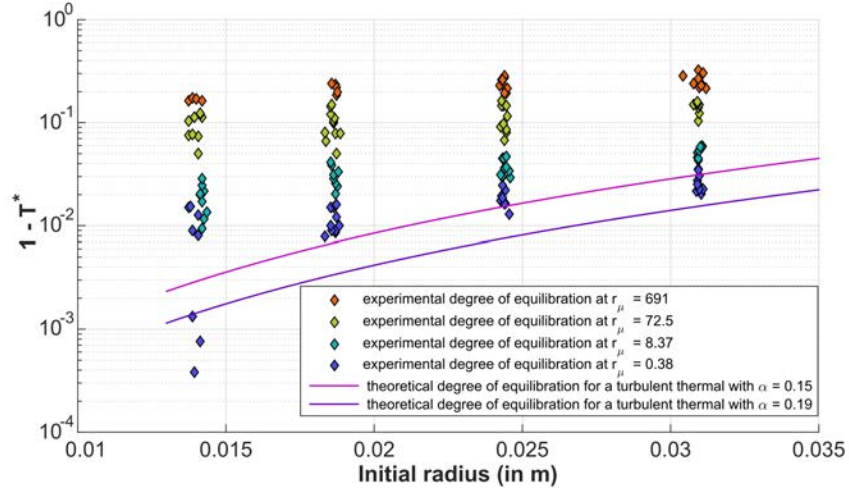


Figure 11: Distance from total equilibration (i.e. 1 minus the experimental degree of equilibration at the bottom of our experiment) from our measurements (symbols) and from the theoretical prediction assuming total equilibration of the liquid metal with the ambient fluid incorporated in the thermal, for both a conservative and the average value of the entrainment coefficient (lines).

410 separating the two. Taking into account the large thermal diffusivity of the
 411 metal and the expected intense flows inside the low viscosity metal drops, we
 412 assume that their interior is well-mixed and at a unique mean temperature
 413 $T(z)$. Consequently, temperature gradients are set by the diffusion in the
 414 boundary layer of size l_{dif} around each drop. Then heat equation writes :

$$\frac{d(V \cdot \rho_m \cdot C_{p_m} \cdot T(z))}{dt} = V \cdot \rho_m \cdot C_{p_m} \cdot u \cdot \frac{dT(z)}{dz} = -S \cdot \lambda_a \cdot \frac{(T(z) - T_{ambient})}{l_{dif}} \quad (11)$$

415 where V is the total volume of metal, C_{p_m} its heat capacity, S the total
 416 metal / ambient fluid surface of exchange, and λ_a the thermal conductivity
 417 of the ambient fluid. The time evolution of the mean metal temperature,

418 or equivalently its depth evolution since the sinking velocity u is constant,
 419 then depends on the heat flux times the surface of exchange, divided by the
 420 (constant) volume of metal. At this point, we don't know the exact evolution
 421 of the surface of exchange as a function of time, which would help to provide
 422 a better model of equilibration. However, since the other parameters can be
 423 considered as constant, we will compute a mean experimental length scale of
 424 equilibration, by implicitly assuming a surface of exchanges averaged along
 425 the fall. With this approximation, the differential equation for the mean
 426 temperature of the liquid metal can be simply written:

$$\frac{dT^*}{dz} = (1 - T^*)/L_{eq} \quad (12)$$

427 whose solution writes

$$T^* = 1 - \exp^{-z/L_{eq}} . \quad (13)$$

428 Here the equilibration length scale is

$$L_{eq} = l_{dif} \cdot \frac{\rho_m \cdot C p_m}{\lambda_a} \cdot u \cdot \frac{V}{S} \quad (14)$$

429 On the basis of our temperature measurements of galinstan at the top and
 430 bottom of the set-up, and using equation (13), we compute the experimental
 431 length scale of equilibration with the following formula:

$$L_{eq} = - \frac{H}{\ln(1 - T^*(H))} \quad (15)$$

432 where H is the total height of the galinstan's fall.

433 The equilibration length scales computed from our experiments are pre-
 434 sented in figure 12. For comparison, the equilibration length scales according

435 to three different models are computed from the theoretical formula (14). Hy-
 436 potheses for these three models are given in table 3, regarding the three key
 437 parameters: the large scale advection speed u , the thickness of the thermal
 438 boundary layer l_{dif} , and the typical ratio of volume over surface area V/S .

439 The first model corresponds to the classical iron rain. It assumes that
 440 equilibration is made between the ambient fluid and drops of laminar cap-
 441 illary size (see equation 9) falling at their terminal velocity (i.e. equation
 442 3 using the laminar capillary size). The size of the thermal boundary layer
 443 l_{dif} is determined by equilibrating advection at the size of the drops with
 444 diffusion through l_{dif} (Samuel, 2012). Besides, the volume to surface ratio is
 445 also given by the laminar capillary size. The corresponding scaling for the
 446 length scale of equilibration is then given in terms of global dimensionless
 447 numbers by

$$L_{eq} = c_1 \frac{Cp_m \cdot \rho_m}{Cp_a \cdot \rho_a} \cdot Pe^{1/2} \cdot We^{-7/8} \cdot R_0 \quad (16)$$

448 where c_1 is a non-dimensional coefficient and $Pe = u.R_0/D_a$ is the Peclet
 449 number of the diapir, $D_a = \lambda_a/\rho_a Cp_a$ being the thermal diffusivity of the
 450 ambient fluid. Interestingly, rewriting L_{eq} in terms of primary parameters,
 451 we find

$$L_{eq} = c_1 \frac{Cp_m \cdot \rho_m}{Cp_a \cdot \rho_a} \cdot \frac{1}{D_a^{1/2}} \cdot \left(\frac{\rho_m - \rho_a}{\rho_a} g \right)^{-5/8} \cdot \left(\frac{\sigma}{\rho_a} \right)^{7/8}, \quad (17)$$

452 hence an equilibration length independent of the initial diapir radius, as well
 453 as of the viscosity of the ambient fluid: within this model, the equilibration
 454 length in our system should be constant over all experimental runs.

455 On the contrary, the two other models take into account the large scale
 456 evolution of the flow as a turbulent thermal, falling at the terminal velocity

457 in the Newton regime of the initial diapir (see section 4.2). Therefore, they
 458 assume that turbulence is fully developed and controls diffusive exchanges.
 459 l_{dif} is determined by equilibrating diffusion with advection at the smallest
 460 advective scale of the turbulent flow, i.e. the Kolmogorov length scale l_{kol}
 461 (see details in Deguen et al., 2014):

$$l_{kol} = R_0 \cdot Re^{-\frac{3}{4}}. \quad (18)$$

462 Assuming a Kolmogorov type turbulence cascade, the velocity fluctuations
 463 u_{kol} at this scale are

$$u_{kol} = u \left(\frac{l_{kol}}{R_0} \right)^{\frac{1}{3}}. \quad (19)$$

464 Hence,

$$l_{dif} = Pe^{-\frac{1}{2}} \cdot Re^{-\frac{1}{4}} \cdot R_0. \quad (20)$$

465 The difference between the two “turbulent thermal” models considered here
 466 comes from the assumption for the interfacial area between the ambient fluid
 467 and the liquid metal. The model developed by Deguen et al. (2014) deals
 468 with the liquid metal in its unbroken form, *i.e.* in its state of crumpled
 469 sheet. It assumes that the interface is advected by an isotropic turbulence
 470 in the same way as an iso-surface of concentration would. The theory of
 471 turbulence then provides the fractal dimension of the interface $D_{fractal} = 8/3$
 472 (see Deguen et al., 2014, for a detailed analysis). The exact value of the
 473 area of the interface between the two fluids is then a unique function of the
 474 cutoff scale l below which the fractal aspect of the interface is lost: $S =$
 475 $4\pi R_0^2 (l/R_0)^{2-D_{fractal}}$. We take for this cutoff length the turbulent capillary
 476 length given by (8), *i.e.* the scale at which surface tension equilibrates the
 477 dynamics pressure due to turbulence. In this framework, the interfacial area

478 scales as

$$S = 4\pi R_0^2 \cdot We^{\frac{2}{5}}. \quad (21)$$

479 Then, the equilibration length is

$$L_{eq} = c_2 \cdot \frac{Cp_m \cdot \rho_m}{Cp_a \cdot \rho_a} \cdot Pe^{\frac{1}{2}} \cdot We^{-\frac{2}{5}} \cdot Re^{-\frac{1}{4}} \cdot R_0 \quad (22)$$

480 where c_2 is a constant, or using the primary parameters

$$L_{eq} = c_2 \frac{Cp_m \cdot \rho_m}{Cp_a \cdot \rho_a} \cdot \frac{1}{\rho_a^{1/4} D_a^{1/2}} \cdot \left(\frac{\rho_m - \rho_a}{\rho_a} g \right)^{-11/40} \cdot \left(\frac{\sigma}{\rho_a} \right)^{2/5} \cdot \mu_a^{1/4} \cdot R_0^{23/40}. \quad (23)$$

481 The last model considered here describes the flow as a turbulent thermal
 482 where the buoyant fluid is a suspension of droplets. The interfacial area is just
 483 the cumulative surface of the drops and the volume to surface ratio should
 484 be well approximated by the mean radius of the drops, corresponding to l_σ
 485 defined by equation (8). Note that we also computed the Sauter diameters
 486 from our size distributions, but it does not show any significant difference
 487 with the above simple approximation, which is thus used for simplicity. Then,
 488 the length scale of equilibration is

$$L_{eq} = c_3 \cdot \frac{Cp_m \cdot \rho_m}{Cp_a \cdot \rho_a} \cdot Pe^{\frac{1}{2}} \cdot We^{-\frac{3}{5}} \cdot Re^{-\frac{1}{4}} \cdot R_0 \quad (24)$$

489 where c_3 is a constant, or using the primary parameters

$$L_{eq} = c_3 \frac{Cp_m \cdot \rho_m}{Cp_a \cdot \rho_a} \cdot \frac{1}{\rho_a^{1/4} D_a^{1/2}} \cdot \left(\frac{\rho_m - \rho_a}{\rho_a} g \right)^{-19/40} \cdot \left(\frac{\sigma}{\rho_a} \right)^{3/5} \cdot \mu_a^{1/4} \cdot R_0^{7/40}. \quad (25)$$

490 The equilibration length for each model is presented in figure 12 together
 491 with the experimental measurements. We focus here on the slope of the
 492 experimental data compared with the slope predicted by the models. The

model description	large scale speed u	thickness of the boundary layer l_{dif}	volume to surface ratio $\frac{V}{S}$
iron rain: stable drops falling at their terminal velocity	terminal velocity of the drops	diffusion equilibrates the laminar advection at the drop scale	laminar capillary length (radius of the stable free falling drops)
turbulent thermal before breakup (Deguen et al., 2014)	terminal velocity in the Newton regime of the initial diapir	diffusion equilibrates the turbulent advection at Kolmogorov scale	fractal surface advected by the turbulence
cloud of droplets evolving as a turbulent thermal	terminal velocity in the Newton regime of the initial diapir	diffusion equilibrates the turbulent advection at Kolmogorov scale	capillary length (radius of the drops)

Table 3: Models tested in this study and their assumptions

493 constants c_1 , c_2 and c_3 have been adjusted for each viscosity ratio to best
494 fit the experimental data. Although the iron rain model is a widely used
495 approximation (Karato and Murthy, 1997; Rubie et al., 2003; Ulvrová et al.,
496 2011; Samuel, 2012), it is incapable of explaining the observed dependence
497 on both the viscosity ratio and the initial radius. In contrast, the turbulent
498 thermal models include a “turbulent” assumption for the thickness of the
499 boundary layer that gives the relevant trend for the influence of the viscosity
500 ratio. Note that this kind of assumption is also used in chemical engineering
501 when considering the mass transfer of bubbly flows in stirred tanks (Petitti
502 et al., 2013). Besides, the iron rain model is based on the value of the falling
503 velocity at the size of one drop, while the two other models consider the
504 global advection speed based on the falling velocity of the initial diapir, in
505 agreement with our experimental results. This explains the dependence of
506 the equilibration length on the initial radius. One could argue that the diapir
507 always breaks up, forms a droplet suspension, and dilutes to a point where
508 the drops fall independently (Bush et al., 2003): the iron rain should then
509 be the relevant asymptotic behaviour. However, our experiments suggest
510 that unless the length scale of initial structures is already on the same order
511 of magnitude as the capillary length, the transient before forming a diluted
512 rain takes place over a significant part of the fall (see additional discussion
513 in Deguen et al., 2011), and that a large part of the equilibration is achieved
514 before the flow is diluted enough to be considered as an iron rain. Therefore
515 it is very unlikely that the iron rain scaling is valid for a post impact flow in
516 planets.

517 It is important to notice that while close, neither the turbulent thermal

518 model nor the turbulent cloud of droplets model actually predicts the correct
519 influence of the diapir initial radius (see figure 12 bottom). We think it is
520 due to the approximation of considering a constant / averaged surface of
521 exchange during the whole fall. Each model is indeed relevant with part
522 of the dynamics only. The crumpled sheet turbulent thermal of Deguen
523 et al. (2014) is well fitted for the flow before the breakup, while the cloud of
524 droplets provides a good description of the flow after the breakup. Hence the
525 measured equilibration length is intermediate between our two estimates. To
526 go any further would require additional experiments, focusing on the time
527 evolution of the surface of exchange, including the initial transient.

528 **6. Conclusion**

529 To conclude, our measurements of thermal exchanges between a liquid
530 metal and an ambient fluid integrated over the fall show a dependence on
531 the viscosity ratio between the two fluids and on the initial size of the diapir.
532 We suggest for advanced models of iron/silicate equilibration the use of the
533 turbulent thermal solution for the dilution of the iron diapir in the magma
534 ocean (Morton et al., 1956; Deguen et al., 2011), and the use of the corre-
535 sponding turbulent scalings for the length scale of equilibration: respectively
536 (22) before the breakup (modified from Deguen et al., 2014), and (24) after
537 the breakup. When building such models, a special attention should be paid
538 when choosing the size of the initial structures as these are still discussed
539 (Kendall and Melosh, 2016) and seem to have a relatively high influence on
540 equilibration. The size of these remnant structures will also determine the
541 initial speed of the liquid metal, which is in our experiment the typical speed

542 of the flow when most of equilibration happens. On the one hand, if one con-
543 sider the remnant structures as the whole core of the planetesimal, it would
544 probably inherit its initial speed from the impact velocity, which should be
545 close to the escape velocity (Dahl and Stevenson, 2010). On the other hand,
546 if the structures are very well diluted after the impact (Kendall and Melosh,
547 2016) or, as recently suggested by Kraus et al. (2015), the iron is vapor-
548 ized upon impact in a large proportion, the initial speed of the metal would
549 probably be the terminal speed of the remnant structures, which obviously
550 depends on their size. In addition, our experiment also suggests that breakup
551 distance should be set to approximately 13 times the size of the initial di-
552 apirs. Since the physics of the exchanges appear to be changing dramatically
553 after the breakup, the size of the initial diapirs is further more important.
554 Finally, future experiments will be required to better characterize the sur-
555 face to volume of the droplets distribution and to quantify the exchanges as
556 a function of depth during the fall, in order to complement the integrated
557 measures made in this study.

7. Acknowledgments

We acknowledge support from the European Research Council (ERC) under the European Union’s Horizon 2020 research and innovation program (grant agreement No. 681835-FLUDYCO-ERC-2015-CoG). We thank our reviewers H. Samuel and R. Deguen for useful comments and interesting discussions, that helped to significantly improve the first version of this paper.

Allègre, C. J., Manhès, G., Göpel, C., Mar. 2008. The major differentiation of the Earth at 4.45 Ga. *Earth and Planetary Science Letters* 267 (1-2),

386–398.

URL <http://linkinghub.elsevier.com/retrieve/pii/S0012821X07007881>

Boujibar, A., Andrault, D., Bouhifd, M. A., Bolfan-Casanova, N., Devidal, J.-L., Trcera, N., Apr. 2014. Metalsilicate partitioning of sulphur, new experimental and thermodynamic constraints on planetary accretion. *Earth and Planetary Science Letters* 391, 42–54.

URL <http://linkinghub.elsevier.com/retrieve/pii/S0012821X14000314>

Bush, J. W. M., Thurber, B. A., Blanchette, F., Jul. 2003. Particle clouds in homogeneous and stratified environments. *Journal of Fluid Mechanics* 489, 29–54.

URL http://www.journals.cambridge.org/abstract_S0022112003005160

Canup, R. M., Apr. 2004. Simulations of a late lunar-forming impact. *Icarus* 168 (2), 433–456.

URL <http://linkinghub.elsevier.com/retrieve/pii/S0019103503002999>

Chambers, J. E., Jul. 2004. Planetary accretion in the inner Solar System. *Earth and Planetary Science Letters* 223 (3-4), 241–252.

URL <http://linkinghub.elsevier.com/retrieve/pii/S0012821X04002791>

Chen, H. T., Middleman, S., Sep. 1967. Drop size distribution in agitated liquid-liquid systems. *AIChE Journal* 13 (5), 989–995.

URL <http://doi.wiley.com/10.1002/aic.690130529>

Clift, R., Grace, J. R., Weber, M. E., 1992. *Bubbles, drops, and particles*, 3rd Edition. Acad. Press, New York, NY, oCLC: 258197988.

- Dahl, T. W., Stevenson, D. J., Jun. 2010. Turbulent mixing of metal and silicate during planet accretion and interpretation of the Hf-W chronometer. *Earth and Planetary Science Letters* 295 (1-2), 177–186.
URL <http://linkinghub.elsevier.com/retrieve/pii/S0012821X10002220>
- Deguen, R., Landeau, M., Olson, P., Apr. 2014. Turbulent metal-silicate mixing, fragmentation, and equilibration in magma oceans. *Earth and Planetary Science Letters* 391, 274–287.
URL <http://linkinghub.elsevier.com/retrieve/pii/S0012821X14000806>
- Deguen, R., Olson, P., Cardin, P., Oct. 2011. Experiments on turbulent metal-silicate mixing in a magma ocean. *Earth and Planetary Science Letters* 310 (3-4), 303–313.
URL <http://linkinghub.elsevier.com/retrieve/pii/S0012821X1100505X>
- Hinze, J. O., Sep. 1955. Fundamentals of the hydrodynamic mechanism of splitting in dispersion processes. *AIChE Journal* 1 (3), 289–295.
URL <http://doi.wiley.com/10.1002/aic.690010303>
- Ichikawa, H., Labrosse, S., Kurita, K., Jan. 2010. Direct numerical simulation of an iron rain in the magma ocean. *Journal of Geophysical Research* 115 (B1).
URL <http://doi.wiley.com/10.1029/2009JB006427>
- Karato, S.-I., Murthy, V. R., Mar. 1997. Core formation and chemical equilibrium in the Earth - I. Physical considerations. *Physics of the Earth and Planetary Interiors* 100 (1-4), 61–79.
URL <http://linkinghub.elsevier.com/retrieve/pii/S0031920196032323>

- Karki, B. B., Stixrude, L. P., May 2010. Viscosity of MgSiO₃ Liquid at Earth's Mantle Conditions: Implications for an Early Magma Ocean. *Science* 328 (5979), 740–742.
URL <http://www.sciencemag.org/cgi/doi/10.1126/science.1188327>
- Kaula, W. M., 1979. Thermal evolution of Earth and Moon growing by planetesimal impacts. *Journal of Geophysical Research* 84 (B3), 999.
URL <http://doi.wiley.com/10.1029/JB084iB03p00999>
- Kendall, J. D., Melosh, H., Aug. 2016. Differentiated planetesimal impacts into a terrestrial magma ocean: Fate of the iron core. *Earth and Planetary Science Letters* 448, 24–33.
URL <http://linkinghub.elsevier.com/retrieve/pii/S0012821X16302217>
- King, C., Olson, P., Apr. 2011. Heat partitioning in metal-silicate plumes during Earth differentiation. *Earth and Planetary Science Letters* 304 (3-4), 577–586.
URL <http://linkinghub.elsevier.com/retrieve/pii/S0012821X11001166>
- Kleine, T., Mezger, K., Palme, H., Münker, C., Nov. 2004. The W isotope evolution of the bulk silicate Earth: constraints on the timing and mechanisms of core formation and accretion. *Earth and Planetary Science Letters* 228 (1-2), 109–123.
URL <http://linkinghub.elsevier.com/retrieve/pii/S0012821X04005679>
- Kolmogorov, A., 1949. On the breakage of drops in a turbulent flow. *Doklady Akademii Nauk SSSR* 66, 825–828.

- Kraus, R. G., Root, S., Lemke, R. W., Stewart, S. T., Jacobsen, S. B., Mattsson, T. R., Mar. 2015. Impact vaporization of planetesimal cores in the late stages of planet formation. *Nature Geoscience* 8 (4), 269–272.
URL <http://www.nature.com/doi/10.1038/ngeo2369>
- Landeau, M., Deguen, R., Olson, P., Jun. 2014. Experiments on the fragmentation of a buoyant liquid volume in another liquid. *Journal of Fluid Mechanics* 749, 478–518.
URL http://www.journals.cambridge.org/abstract_S002211201400202X
- Lasheras, J. C., Villermaux, E., Hopfinger, E. J., 1998. Break-up and atomization of a round water jet by a high-speed annular air jet. *Journal of Fluid Mechanics* 357, 351–379.
URL http://journals.cambridge.org/abstract_S0022112097008070
- Lee, D., Halliday, A., Dec. 1996. Hf-W Isotopic Evidence for Rapid Accretion and Differentiation in the Early Solar System. *Science (New York, N.Y.)* 274 (5294), 1876–1879.
- Merk, R., Breuer, D., Spohn, T., Sep. 2002. Numerical Modeling of 26 Al-Induced Radioactive Melting of Asteroids Considering Accretion. *Icarus* 159 (1), 183–191.
URL <http://linkinghub.elsevier.com/retrieve/pii/S0019103502968727>
- Monteux, J., Coltice, N., Dubuffet, F., Ricard, Y., Dec. 2007. Thermo-mechanical adjustment after impacts during planetary growth. *Geophysical Research Letters* 34 (24).
URL <http://doi.wiley.com/10.1029/2007GL031635>

- Morton, B. R., Taylor, G., Turner, J. S., 1956. Turbulent gravitational convection from maintained and instantaneous sources. In: Proceedings of the Royal Society of London A: Mathematical, Physical and Engineering Sciences. Vol. 234. The Royal Society, pp. 1–23.
URL <http://rspa.royalsocietypublishing.org/content/234/1196/1.short>
- Neumann, W., Breuer, D., Spohn, T., Jul. 2012. Differentiation and core formation in accreting planetesimals. *Astronomy & Astrophysics* 543, A141.
URL <http://www.aanda.org/10.1051/0004-6361/201219157>
- O'brien, D., Morbidelli, A., Levison, H., Sep. 2006. Terrestrial planet formation with strong dynamical friction. *Icarus* 184 (1), 39–58.
URL <http://linkinghub.elsevier.com/retrieve/pii/S0019103506001278>
- Petitti, M., Vanni, M., Marchisio, D. L., Buffo, A., Podenzani, F., Jul. 2013. Simulation of coalescence, break-up and mass transfer in a gasliquid stirred tank with CQMOM. *Chemical Engineering Journal* 228, 1182–1194.
URL <http://linkinghub.elsevier.com/retrieve/pii/S1385894713006670>
- Reese, C., Solomatov, V., Sep. 2006. Fluid dynamics of local martian magma oceans. *Icarus* 184 (1), 102–120.
URL <http://linkinghub.elsevier.com/retrieve/pii/S0019103506001308>
- Rubie, D., Melosh, H., Reid, J., Liebske, C., Righter, K., Jan. 2003. Mechanisms of metal-silicate equilibration in the terrestrial magma ocean. *Earth and Planetary Science Letters* 205 (3-4), 239–255.
URL <http://linkinghub.elsevier.com/retrieve/pii/S0012821X02010440>

Safronov, V. S., 1978. The heating of the Earth during its formation. *Icarus* 33 (1), 3–12.

URL <http://www.sciencedirect.com/science/article/pii/0019103578900192>

Samuel, H., Jan. 2012. A re-evaluation of metal diapir breakup and equilibration in terrestrial magma oceans. *Earth and Planetary Science Letters* 313-314, 105–114.

URL <http://linkinghub.elsevier.com/retrieve/pii/S0012821X11006406>

Samuel, H., Tackley, P., Evonuk, M., Feb. 2010. Heat partitioning in terrestrial planets during core formation by negative diapirism. *Earth and Planetary Science Letters* 290 (1-2), 13–19.

URL <http://linkinghub.elsevier.com/retrieve/pii/S0012821X09007122>

Stevenson, D., 1990. Fluid dynamics of core formation. *Origin of the Earth* 1, 231–249.

Tonks, W. B., Melosh, H. J., Dec. 1992. Core formation by giant impacts. *Icarus* 100 (2), 326–346.

URL <http://linkinghub.elsevier.com/retrieve/pii/001910359290104F>

Ulvrová, M., Coltice, N., Ricard, Y., Labrosse, S., Dubuffet, F., Velínský, J., Šrámek, O., Oct. 2011. Compositional and thermal equilibration of particles, drops, and diapirs in geophysical flows. *Geochemistry, Geophysics, Geosystems* 12 (10).

URL <http://doi.wiley.com/10.1029/2011GC003757>

Villiermaux, E., Pistre, V., Lhuissier, H., Sep. 2013. The viscous Savart

sheet. *Journal of Fluid Mechanics* 730, 607–625.

URL http://www.journals.cambridge.org/abstract_S0022112013003546

Wacheul, J.-B., Le Bars, M., Monteux, J., Aurnou, J. M., Oct. 2014.

Laboratory experiments on the breakup of liquid metal diapirs. *Earth and Planetary Science Letters* 403, 236–245.

URL <http://linkinghub.elsevier.com/retrieve/pii/S0012821X1400435X>

Yoshino, T., Walter, M. J., Katsura, T., Mar. 2003. Core formation in plan-

etesimals triggered by permeable flow. *Nature* 422 (6928), 154–157.

URL <http://www.nature.com/doi/10.1038/nature01459>

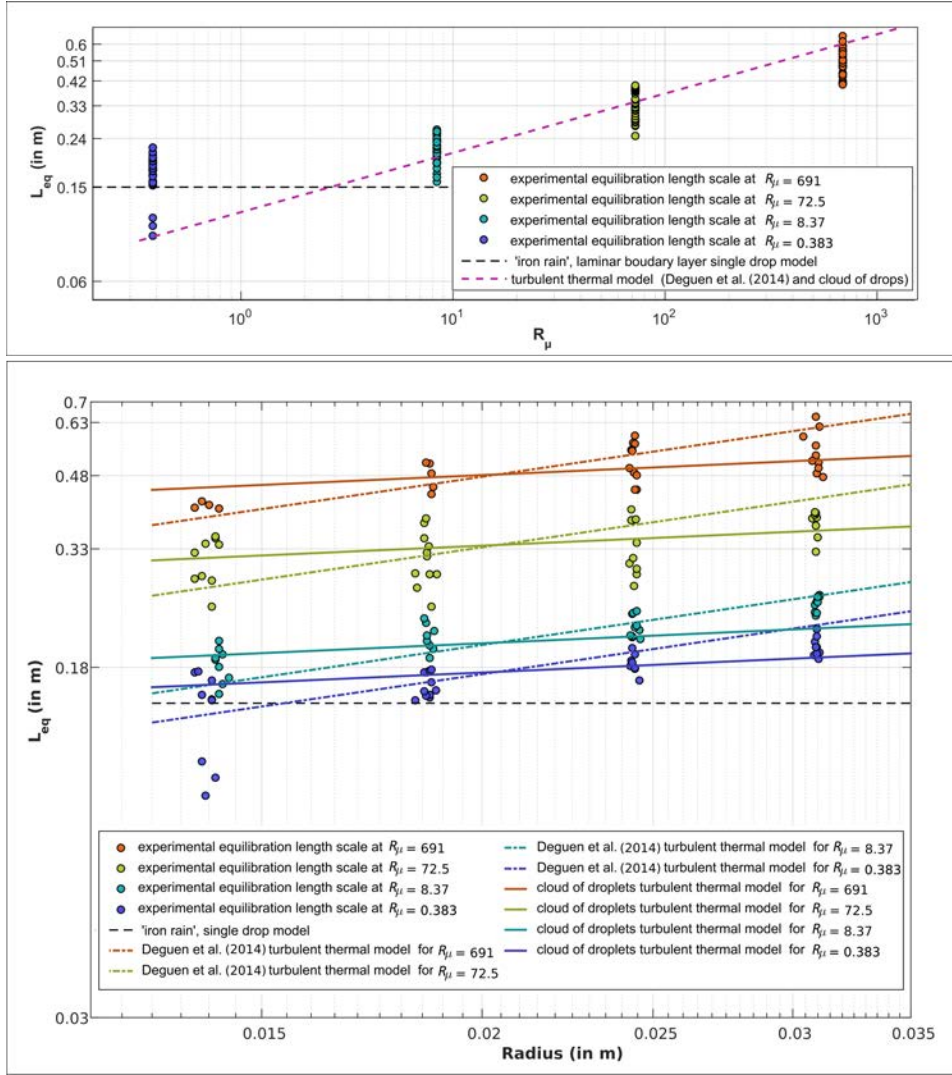


Figure 12: Top: experimental equilibration lengths (circles) and equilibration lengths computed according to the “iron rain” (black dashed line) and turbulent thermal models (fuchsia dashed line) plotted as a function of the viscosity ratio. Bottom: experimental equilibration lengths (circles) and equilibration lengths computed according to the “iron rain” model (black dashed line), the turbulent thermal model of Deguen et al. (2014) (dashed dotted lines), and the cloud of droplet turbulent thermal model (solid lines), plotted as a function of the initial diapir radius.